AIAA SciTech Forum
January 3-7, 2022, San Diego, CA & Virtual
AIAA SCITECH 2022 Forum
10.2514/6.2022-2420

Wing Dynamic Shape-Sensing From Fiber-Optic Strain Data Using the Kalman State Estimator

Tsoof Joels * and Daniella E. Raveh†
Technion—Israel Institute of Technology, 3200000 Haifa, Israel

A novel method for shape sensing based on strain data and the use of the Kalman state estimator is presented and studied experimentally. Several recent studies proposed different methods in which strain data, measured in optical fibers, can be used to estimate the deformed shape of a flexible wing. Fiber optic sensors typically provide accurate, high resolution, strain data, yielding detailed prediction of a wing's deformed shape. However, in real lift applications there could be moments in which the strain data is imperfect (for example, due to saturation), or altogether missing. The current study proposed to use a Kalman state estimator that weighs in strain-data and simulation output of an aeroelastic plant model to estimate the wing deformations. The method is demonstrated with a flexible wing model that is excited by prescribed control surfaces deflection in a wind-tunnel test. Strains over the front and rear wing spars are measured by Fiber Bragg Grating sensors, embedded in two optical fibers, and used to estimate the wing deformations. The latter are compared to wing deformations measured by a motion recovery camera system. Results show the advantageous of the use of the Kalman state estimator when the strain data is corrupted. Additionally, with this approach, wing's modal velocities are estimated together with the wing deformations, resulting in smooth and accurate modal velocities that are readily usable by the vehicle's control system.

I. Introduction

New aircraft designs are more flexible than ever before, making them susceptible to adverse aeroelastic phenomena such as large dynamic response to atmospheric turbulence and flutter instability. On the other hand, some studies suggest that wing elasticity can be exploited to achieve optimal performance. To either control aeroelastic responses or leverage them for performance requires information on wing deformations.

Wing elastic deformation is typically measured and expressed in terms of wingtip displacement [1], or modal deformation [2, 3]. The former can be obtained from accelerometer measurements using time integration. However, this information is local and typically limited to a few points. Recent studies have shown that a detailed deformed shape of a structure could be obtained from strain data measured in optical fibers (e.g., [4–6].)

Fiber-optic sensing has seen an increased acceptance, as well as widespread use, in civil engineering, aerospace, marine, and oil and gas. A prominent use of fiber-optic sensors (FOS) in the aerospace industry is for structural health monitoring of complex aero-structures. Their inherent capabilities, including strain accuracy comparable with that of standard electrical strain-gauges [7], high sensitivity and wide strain dynamic range, high sampling rate (kHz for point sensing), multiplexed operation (one fiber can support many sensors), insensitivity to electromagnetic radiation, small size and light weight, make FOS highly suitable for aerospace systems. For the same reasons, FOS are also very attractive for aeroelastic applications that require shape-sensing.

Currently, there are three methods used to translate measured strains to deformations. Based on the Euler Bernoulli beam theory, Ko's method [8] double integrates strains measured along a line (e.g., a line over a wing's span) to compute the deformation. The drawbacks of Ko's method are mainly the numerical integration, which accumulates errors, and the need for information on the distance between the measurement point and the neutral axis, which is not readily available in complex structures. The inverse finite-element method (IFEM) [9] is based on a discretized finite-element representation of a structure and formulation of the strain field in terms of nodal displacements. The latter are found by minimizing the difference between the computed and measured strains. The IFEM was successfully used in different applications. [5, 10] Its disadvantages are that it requires an additional, dedicated finite-element (FE) model, and a significantly large set of strain data for accurate displacement prediction.

A modal method, first suggested by Foss and Huagse [11], represents the measured strains as a combination of strain modes, and a least-squares (LS) technique is used to compute the modal participation coefficients (modal amplitudes). The same modal amplitudes, when multiplying the deformation modes, provide the deformed shape. The strain and displacement modes can be determined from a FE model free-vibration analysis or extracted from a ground vibration

*Graduate Student, Faculty of Aerospace Engineering, Technion, AIAA Member, tsoof@campus.technion.ac.il
†Professor, Faculty of Aerospace Engineering; daniella@technion.ac.il. Associate Fellow AIAA

test (GVT). Recently, Freydin et al. [6] demonstrated the successful use of the method for measuring the static and dynamic deformed shape of a flexible wing in a wind-tunnel test. It was shown that when high-quality strain data is available, as is typically the case with FOS, a very accurate reconstruction of the displacements can be achieved. In realistic flight applications, however, the accuracy of the displacements prediction can deteriorate if the strain data is inexact (for example, due to temperature effects or sensor saturation), or missing, or if the modal model used for the strain-to-displacement mapping is inaccurate.

In the current study, we propose a new approach to wing shape-sensing that is based on an approximate model of the system, including displacement and strain modes, measured strain-data, and the use of the Kalman state-estimator (KSE). The KSE estimates the system's states, some of which are the modal amplitudes. From the latter, and with the displacement- and strain-modes available, future values of the strains and displacements can be predicted. The KSE minimizes the LSQ error of state estimation by accounting for the system's predicted state and measurements and while considering possible errors in the model and data through the covariance of process and measurement noises. [12] The advantages of using the KSE for strain-to-displacement mapping are that 1) It does not require an accurate model of the system; 2) It is insensitive to measurement errors, noise, or temporarily missing data (e.g., due to sensor saturation); 3) It provides the state velocities (i.e., modal velocities) without the need for numerical derivation of the deformations, and 3) It can provide the deformation information in real-time.

For a flexible structure, without the presence of airloads, the required state-space model can be derived from a finite-element model. This was successfully demonstrated by Palanisamya et al. [13] in estimation of strains in various locations along a beam based on a finite-element model and limited strain measurements, acceleration and tilt data. For an aircraft in flight, or a wind-tunnel model, an aeroelastic state-space model can be derived by using rational function approximations for the unsteady aerodynamics. [14] Such a model is dependent on the flight conditions and varies with them.

In the current study, the proposed method is demonstrated experimentally in a wind-tunnel test of a flexible wing model with four control surfaces. The modal and physical deformations in response to initial conditions and forced excitation (via the control surfaces) are computed using a KSE from FOS-recorded strain data and an aeroelastic model of the wing. The estimated deformations are compared with those measured by an Infra-red (IR) Motion Recovery System (MRS). The study examines the performance of the prediction system in a nominal case and in cases where 1) the strain data is effected by saturation 2) the aeroelastic model is inaccurate (computed for an airspeed different than the test airspeed. The study also examines the accuracy of the predicted deformations when using modes from a FE model versus modes extracted experimentally in a GVT.

II. Mathematical Model

Following [14], the state-space model of the aeroelastic plant, subject to control-surface excitation input and accounting for noise, can be written as

$$\begin{aligned} \dot{\boldsymbol{x}} &= \boldsymbol{A}\boldsymbol{x} + \boldsymbol{B}\boldsymbol{u} + \boldsymbol{w} \\ \boldsymbol{y} &= \boldsymbol{C}\boldsymbol{x} + \boldsymbol{v}, \end{aligned} \tag{1}$$

where $\boldsymbol{x} = [\boldsymbol{\xi}, \dot{\boldsymbol{\xi}}, \boldsymbol{X_a}, \boldsymbol{\delta}, \dot{\boldsymbol{\delta}}, \ddot{\boldsymbol{\delta}}]$ is the state vector, in which $\boldsymbol{\xi}$ and $\dot{\boldsymbol{\xi}}$ are the vectors of n_m generalized displacements and their time derivatives, $\boldsymbol{X_a}$ is the vector of n_a augmented aerodynamic states, and $\boldsymbol{\delta}$,$\dot{\boldsymbol{\delta}}$, and $\ddot{\boldsymbol{\delta}}$ are the vectors of n_{cs} control-surface deflections and their time derivatives. $\boldsymbol{u}$ holds the n_{cs} control-surface deflection commands $\boldsymbol{u} = \boldsymbol{\delta}_{com}$, and $\boldsymbol{w}$ and $\boldsymbol{v}$ are the process and measurement noise vectors. The aeroelastic plant's matrices $\boldsymbol{A}$ and $\boldsymbol{B}$ are derived in [14]. The output vector $\boldsymbol{y}$ holds the n_s strains, $\boldsymbol{\varepsilon}$, which are related to the generalized displacements through the strain-mode matrix $\boldsymbol{\Psi}$, as

$$\boldsymbol{\varepsilon} = \boldsymbol{\Psi}\boldsymbol{\xi}. \tag{2}$$

The output matrix $\boldsymbol{C}$ is therefor

$$\boldsymbol{C} = \begin{bmatrix} \boldsymbol{\Psi}_{n_s,n_m} & \boldsymbol{0}_{n_s,(n_m+n_a+3\times n_{cs})} \end{bmatrix}. \tag{3}$$

As noted in the introduction, a common approach to extracting modal displacements from strain data is based on a LSQ process that seeks the combination of (pre-known) strain modes, according to Equation (2), that best captures the measured strain data [6, 11, 15]. When high quality strain-data is available, the modal displacements $\boldsymbol{\xi}$ can be estimated as:

$$\boldsymbol{\xi} = [\boldsymbol{\Psi}^T\boldsymbol{\Psi}]^{-1}\boldsymbol{\Psi}^T\boldsymbol{\varepsilon}, \tag{4}$$

from which the physical displacements, z can be computed as

$$z = \mathbf{\Phi}\boldsymbol{\xi}, \tag{5}$$

where $\mathbf{\Phi}$ is the matrix of displacement modes. Matrices $\mathbf{\Phi}$ and $\mathbf{\Psi}$ can be computed from a FE model free-vibration analysis or computationally extracted from a GVT. For cases in which the strain data is imperfect, the KSE can be used to estimate the generalized and physical displacements based on a weighted combination of the data and the model.

The discrete-time form of the system in Eq. 1, for any data point k is:

$$\begin{aligned} \boldsymbol{x_k} &= \tilde{\boldsymbol{A}}\boldsymbol{x_{k-1}} + \tilde{\boldsymbol{B}}\boldsymbol{u_{k-1}} + \boldsymbol{w_{k-1}} \\ \boldsymbol{y_k} &= \boldsymbol{C}\boldsymbol{x_k} + \boldsymbol{v_k}, \end{aligned} \tag{6}$$

where $\tilde{\boldsymbol{A}}$ and $\tilde{\boldsymbol{B}}$ can be computed from eq. (1):

$$\tilde{\boldsymbol{A}} = \boldsymbol{A}\Delta t + \boldsymbol{I} \tag{7}$$

$$\tilde{\boldsymbol{B}} = \boldsymbol{B}\Delta t. \tag{8}$$

The KSE predictor equation computes the predicted $k+1$ state vector based on all previous k data points, as

$$\hat{\boldsymbol{x}}_{\boldsymbol{k+1|k}} = \tilde{\boldsymbol{A}}\hat{\boldsymbol{x}}_{\boldsymbol{k|k}} + \tilde{\boldsymbol{B}}\boldsymbol{u_k}. \tag{9}$$

The corrector equation uses the k+1 measurement, $\boldsymbol{\varepsilon_{k+1}}$, and the KSE Gain matrix, $\boldsymbol{K_{k+1}}$, to compute $\boldsymbol{x_{k+1|k+1}}$, the estimated state vector $\boldsymbol{x}$ at time k+1 according to

$$\hat{\boldsymbol{x}}_{\boldsymbol{k+1|k+1}} = \hat{\boldsymbol{x}}_{\boldsymbol{k+1|k}} + \boldsymbol{K_{k+1}}(\boldsymbol{\varepsilon_{k+1}} - \boldsymbol{C}\hat{\boldsymbol{x}}_{\boldsymbol{k+1|k}}). \tag{10}$$

The KSE gain, $\boldsymbol{K_{k+1}}$, can be expressed as:

$$\boldsymbol{K_{k+1}} = \left[\boldsymbol{P_{k+1|k}}\boldsymbol{C^T}\left[\boldsymbol{C}\boldsymbol{P_{k+1|k}}\boldsymbol{C^T} + \boldsymbol{R}\right]^{-1}\right] \tag{11}$$

where $\boldsymbol{R}$ is the measurement noise covariance matrix and $\boldsymbol{P}$ is the steady-state error covariance matrix. The latter is obtained by solving the algebraic Riccati equation that uses the process noise covariance $\boldsymbol{Q}$ [13].

$$\boldsymbol{P_{k+1|k}} = [\tilde{\boldsymbol{A}}\boldsymbol{P_{k|k}}\tilde{\boldsymbol{A}}^{\boldsymbol{T}} + \boldsymbol{Q}] \tag{12}$$

$$\boldsymbol{P_{k+1|k+1}} = (\boldsymbol{I} - \boldsymbol{K_{k+1}}\boldsymbol{C})\boldsymbol{P_{k+1|k}} \tag{13}$$

We next show that when the measured strain data is perfect, that is, when $\boldsymbol{R} \longrightarrow 0$, predicting the modal displacements using the KSE is equivalent to using a LSQ procedure (Eq. 4). From Equation (11), for any time point k:

$$\boldsymbol{K_k} = [\boldsymbol{C^T}\boldsymbol{C}]^{-1}\boldsymbol{C^T} \tag{14}$$

However,

$$\boldsymbol{C^T}\boldsymbol{C} = \begin{bmatrix} \mathbf{\Psi}^{\boldsymbol{T}}\mathbf{\Psi} & \mathbf{0} \\ \mathbf{0} & \mathbf{0} \end{bmatrix} \tag{15}$$

is a singular matrix that cannot be inverted. We divide matrix $\boldsymbol{K_k}$ into two parts,

$$\boldsymbol{K_k} = \begin{bmatrix} \boldsymbol{K_{1_{n_m,n_s}}} \\ \boldsymbol{K_2} \end{bmatrix} \tag{16}$$

where $\boldsymbol{K_1}$ holds the first n_m lines of $\boldsymbol{K_k}$, and $\boldsymbol{K_2}$ are the rest of $\boldsymbol{K_k}$ lines. From eq. (16) and eq. (14)

$$\boldsymbol{K_1} = [\mathbf{\Psi}^{\boldsymbol{T}}\mathbf{\Psi}]^{-1}\mathbf{\Psi}^{\boldsymbol{T}}. \tag{17}$$

Assigning $\boldsymbol{K}$ (Equation (16)) and $\boldsymbol{C}$ (Equation (3)) to Equation (10) we get

$$\hat{\boldsymbol{x}}_{\boldsymbol{k+1|k+1}} = \hat{\boldsymbol{x}}_{\boldsymbol{k+1|k}} + \begin{bmatrix} \boldsymbol{K_1} \\ \boldsymbol{K_2} \end{bmatrix} \boldsymbol{\varepsilon_{k+1}} - \begin{bmatrix} \boldsymbol{K_1} \\ \boldsymbol{K_2} \end{bmatrix} \begin{bmatrix} \mathbf{\Psi} & \mathbf{0} \end{bmatrix} \hat{\boldsymbol{x}}_{\boldsymbol{k+1|k}}, \tag{18}$$

from which

$$\hat{\xi}_{k+1|k+1} = \hat{\xi}_{k+1|k} + K_1 \varepsilon_{k+1} - K_1 \Psi \hat{\xi}_{k+1|k}. \tag{19}$$

Assigning K_1 from Equation (17) we get the LSQ solution.

Using the KSE for displacements prediction has several advantages:

1) In times of missing or faulty measurements, for example, as a result of sensor saturation, the KSE can rely on the aeroelastic model to provide continuous modal displacement and velocities estimates. The weighting between model and measurement is done at each time step by updating the KSE parameters Q and R, as shown in the test case.
2) The KSE relies on the system's dynamic model (matrices A and B), which is dependent on the flight dynamic pressure. Since the KSE also relies on measured data, the model does not have to be accurate to yield good displacement estimates.
3) When using the LSQ procedure, the modal displacements at each time step are computed from the same time's measurements, independent of the dynamics and past values of the displacements (Equation (4)). Modal velocities, $\dot{\xi}$, can be computed by time derivation of the modal displacements time history. However, this makes the modal velocities highly sensitive to measurement noise. The KSE computes the modal displacements and velocities simultaneously, thus avoiding the noisy modal velocities associated with the LSQ approach. This makes the KSE method especially useful for control systems that rely on modal velocities data.

Both the KSE and the LSQ methods rely on a known set of strain modes of the system (Eqs. 3 and 4). The strain modes can be computed from a FE model of the system, in a free-vibration analysis, or extracted from a GVT in which strains are measured. The advantage of the latter is that the process is data-based, avoiding modeling errors. To estimate the displacements in physical DOFs, a set of displacement modes is also required, from either a FE model or GVT. We examine the effect of using FE or GVT modes on the modal and physical displacement estimates.

In a GVT, the displacement and mode shapes are extracted from the time histories of displacement and strain responses to initial conditions. In the current study, this is done by Spectral Proper Orthogonal Decomposition (SPOD) [16]. The displacement and strain modes are extracted jointly, such that their scaling is uniform. They are compared to modes from FE analysis for validation.

III. Test Case

The proposed shape-sensing method was studied in a wind tunnel test of the flexible wing shown in Figure 1. The 100 mm chord, 600 mm span, NACA 0012 airfoil wing is 3D-printed from Nylon-12 material. It has four trailing edge flaps, controlled with micro-servo actuators, which in the current study are used for excitation input. At the wingtip, a 300mm long and 10mm diameter rod is used for attaching weights to modify the wing's dynamic properties. The wing was tested in the subsonic wind tunnel at the Faculty of Aerospace Engineering, Technion. The wind tunnel has section of 1m by 1m and can run at airspeeds up to 100 m/s. The wing was connected directly to the wind tunnel floor, as showed in Figure 1(b).

For strain measurement, two optical fibers were embedded in cavities in the front and rear spars, on one side of the wing. Fiber Bragg Grating (FBG) sensors were used to measure strains in 15 equally spaced locations on each spar (Table 1). Figure 2 shows the glowing FOS on the front and rear spars, indicating their locations. In the current study, only the strains from sensors number 1,4,7, and 10 on each spar were used for shape sensing, while the other strain measurements were used for validation.

The reference wing shape was measured with the MRS, by 30 IR reflectors placed on the spars and the trailing-edge. Two additional reflectors were located at the wingtip rod ends, 605 mm from the wing root. The IR reflectors are shown in Figure 1 and their locations are provided in Table 2.

The wing structure was modeled in NX NASTRAN FE software [17]. The model was calibrated to match the natural frequencies as measured in a GVT. Table 3 provides the structural frequencies from the calibrated FE model compared with the GVT data. Figures 3 and 4 show the first four low-frequency strain and displacement modes, comparing the computational (FE) and experimental (GVT) shapes. The experimental mode shapes were extracted from the response to initial conditions (strain / displacement response for the strain / displacement modes, respectively) by SPOD [16] analysis. All mode shapes were normalized to a unit max strain. Figures 3 and 4 show an overall similarity between the computational and experimental mode shapes, with some localized discrepancies mostly at the displacement modes that could be possibly attributed to tracking errors of the MRS.

The aerodynamic model was realized in ZAERO using the ZONA6 panel method [18]. The aeroelastic plant state-space matrices, A and B in Equation (1), were computed by ZAERO for the nominal test airspeed of 20 m/s.

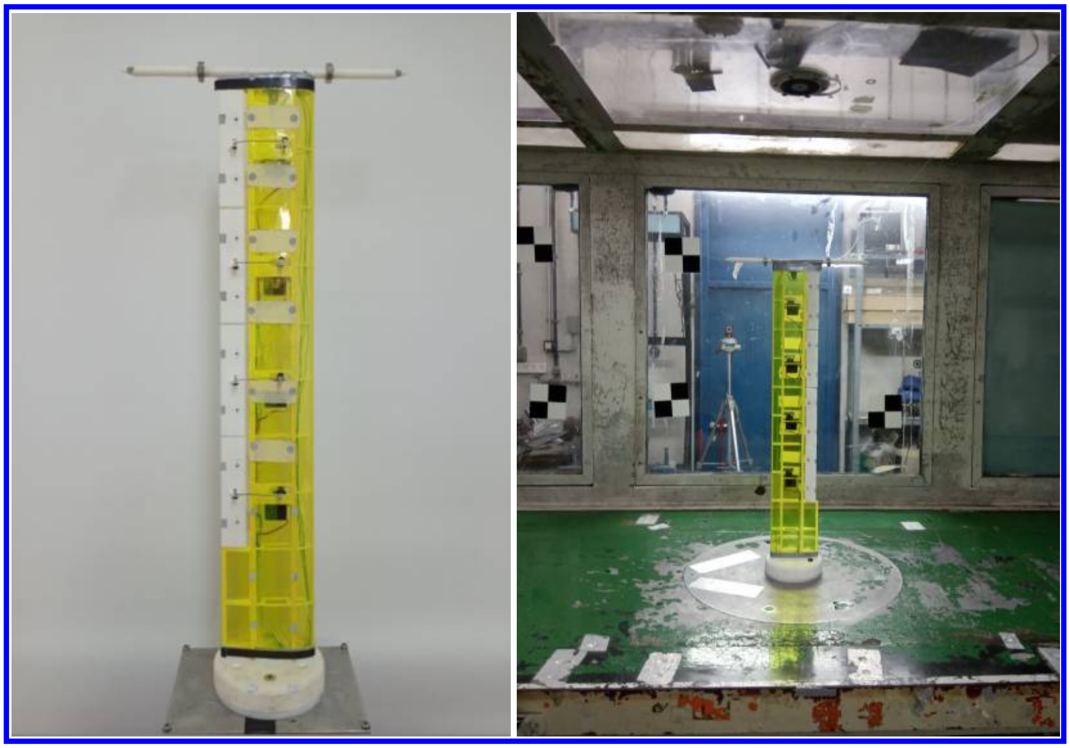

(a) (b)

Fig. 1 Wing model outside (a) and inside the wind tunnel (b)

Table 1 Strain sensor locations along the main and rear spars. Distances measured from the wing root

FOS Position	1	2	3	4	5	6	7	8	9	10	11	12
Main Spar (mm)	20	55	90	125	160	195	230	265	300	335	370	405
Rear Spar (mm)	20	55	90	125	160	195	230	265	300	335	370	405

FBG Position	13	14	15
Main Spar (mm)	440	475	510
Rear Spar (mm)	440	475	510

Table 2 MRS reflector locations along the main and rear spars and the trailing edge. Distances measured from the wing root

Reflector Position	1	2	3	4	5	6	7	8	9	10
Main Spar (mm)	33	86	154	223	282	367	440	504	564	605
Rear Spar (mm)	33	86	154	223	282	367	440	504	564	605
Trailing Edge (mm)	140	200	262	322	382	440	504	564		

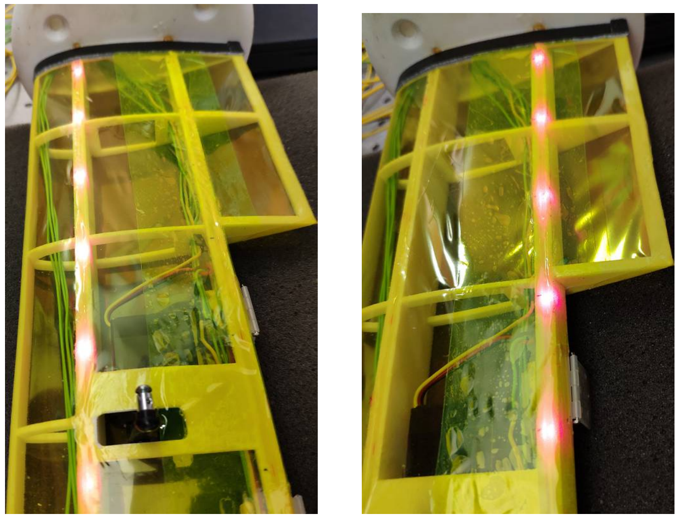

(a) Front Spar (b) Rear Spar

Fig. 2 Glowing FOS showing the sensor locations on the front (a) and rear (b) spars

Table 3 Structural frequencies from the FE model and GVT.

Mode	Description	FE model (Hz)	GVT (Hz)
1	1st bending	4.47	4.48
2	1st torsion	18.7	18.0
3	1st lateral bending	22.4	22.0
4	2nd bending	29.6	29.7

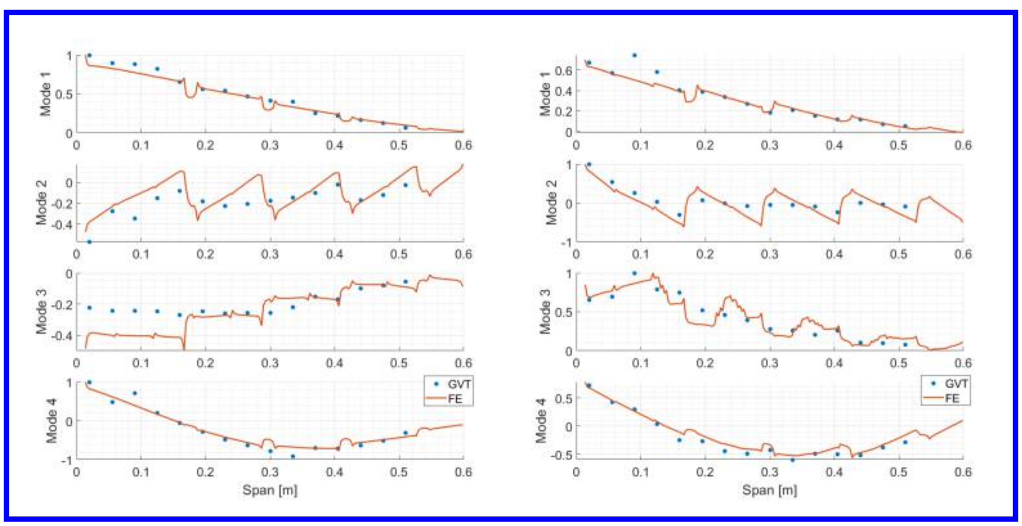

(a) Main Spar (b) Rear Spar

Fig. 3 Strain modes from FE free-vibration analysis and from GVT

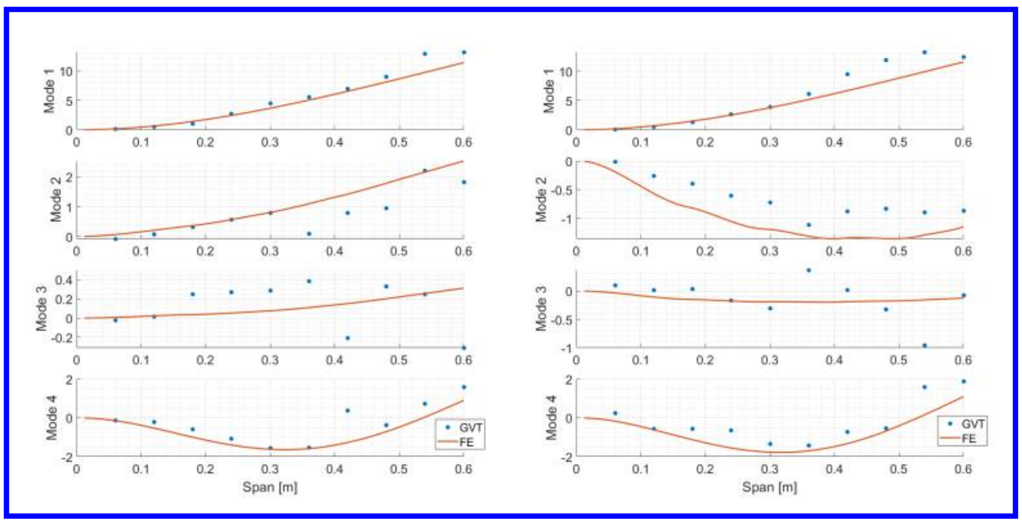

(a) Main Spar

(b) Rear Spar

Fig. 4 Displacement modes from FE free-vibration analysis and from GVT

A. Kalman State-Estimator (KSE) Parameters

$\boldsymbol{R}$ and $\boldsymbol{Q}$ in the KSE gain (Equations (11) and (12)) are the measurement- and process-noise covariance matrices, respectively. They are initially set to unit matrices for equal weighing of the computational model and measurements. At times of poor strain measurements, or when there is a mismatch between the airspeed and the nominal airspeed (for which the aeroelastic model was generated), the terms of matrices $\boldsymbol{R}$ or $\boldsymbol{Q}$ are increased, respectively, to express the reduced level of confidence in the measurements or model.

Poor readings in the strain sensors could be due to saturation or due to sensor failure. As noted, in the current study, only strain measurements from sensors 1,4,7, and 10 on each spar (see their locations in Table 1) are used to estimate the modal displacements. The KSE algorithm is set to switch the faulty sensor's noise covariance term, $\boldsymbol{R_{i,i}}$, to a value of 100 in case the sensor constantly outputs the maximum measurable value (i.e., it is saturated) or a value of zero (i.e., the sensor failed).

When the airspeed is different from the nominal, for which the aeroelastic plant state-space equations were derived, Q_{11} and Q_{44}, associated with the first and second bending modes, are set to

$$Q_{i,i} = 500\frac{|V_{nom} - V|}{V_{nom}}, \tag{20}$$

where V_{nom} and V are the nominal and true airspeeds, respectively, and i equaLSQ 1 and 4.

As the KSE gain is recomputed at each time step, the $\boldsymbol{R}$ and $\boldsymbol{Q}$ values can be updated at each time. The values used here are only suggested values that highlight the usefulness of the KSE in displacement estimation in cases of measurement or process noise. They can be optimized per case, or be set according to a more elaborate switching algorithm.

IV. Results

A. Structural Response to Initial Conditions

As a first test of the KSE-based method, a response to a hammer hit (impulse) at the wingtip was recorded simultaneously with the FOS and MRS. The strain data measured in sensors 1, 4, 7, and 10 on each spar were used to compute the modal displacements, which were compared to those from the LSQ approach. The modal displacements were transformed to physical displacements and compared to displacements detected with the MRS.

Figures 5 and 6 show the modal displacements of the first four modes (ξ_1 - ξ_4) and their time derivatives ($\dot{\xi}_1$ - $\dot{\xi}_4$), as computed from strain-data by LSQ and the KSE. Both are based on the experimental strain modes (Figure 3). Since all strain modes were normalized similarly, to a maximum strain of one, the modal displacements reflect the relative mode's contribution to the total strain. For the larger contributors, ξ_1 and ξ_2, Figure 5 shows a very good match between LSQ and KSE computed modal displacements. There are somewhat more significant differences in the lateral and second out-of-plane bending modal displacements, ξ_3 and ξ_4, whose contributions are an order of magnitude smaller, mainly when these responses decay to small values. The differences in the torsion mode response in the first ≈ 0.2 seconds are due the fact that the hammer hit was not a strict bending impulse. It also induced a torsional motion, captured by the strain data and, therefore, by the LS. The KSE, which weighs the model and data, required ≈ 0.2 seconds to acquire the correct response. Finally, we note that the KSE modal displacements closely follow the decaying response even though the structural model does not account for damping. Figure 6 shows the advantage of the KSE that predicts smooth modal velocity responses compared to the noisy responses obtained from time derivation of the modal displacements computed by LSQ.

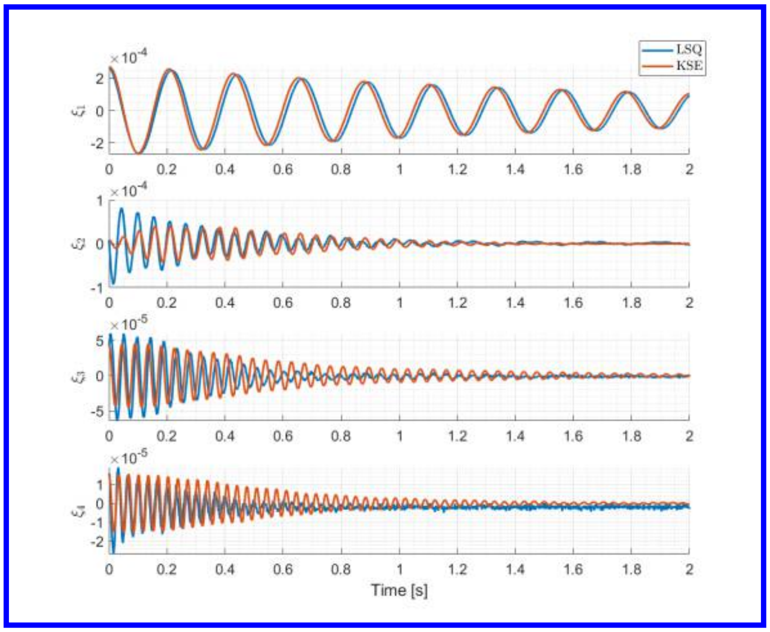

Fig. 5 Modal displacements estimate

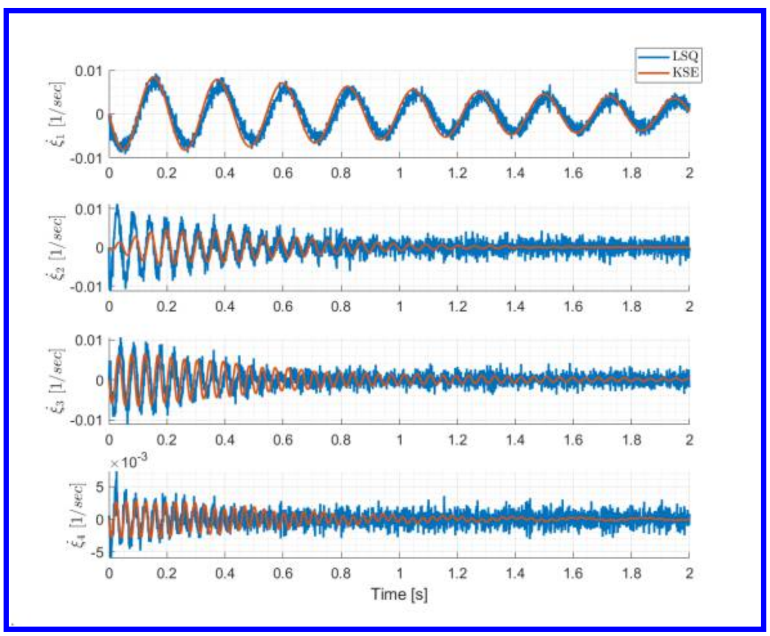

Fig. 6 Modal velocities estimate

Figure 7 shows the estimated and measured strains at sensors #2 on the main and rear spars. These sensors are close to the root but did not participate in the modal displacement estimate (which was based on sensors 1, 4, 7, and 10 on each spar). Figure 8 shows a snapshot of the strain distribution over the wing's main and rear spars at time 1 (s). Figures 7 and 8 show that the LSQ and KSE processes can accurately estimate strain values at unmeasured locations. Mapping of the strains to the whole wing is based on the experimental strain modes. It has the advantage that the strain reconstruction captures local strains, as seen in the rear spar near 100 mm span station.

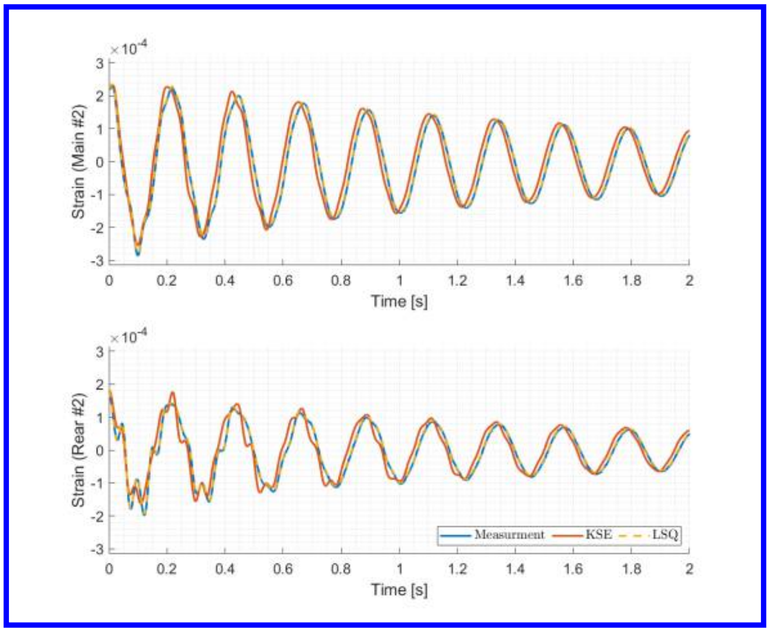

Fig. 7 Estimated strains at unmeasured locations

Figure 9 shows the estimated and measured (via MRS) wingtip displacements at the main- and rear-spar in time and Figure 10 shows the deformed main- and rear-spars at time 1 second. The modal displacements were computed based on the experimental strain modes but the transformation from modal to physical displacements (Equation (5)) uses the FE displacement modes. We assume that the FOS are embedded in the structure, thus experimental strain modes can be obtained from GVT. On the other hand, the displacement modes are not necessarily available from GVT, thus the computational modes are used. For this case, the process results in good match between the estimated (both via LSQ and the KSE) and measured wingtip displacements. We note that the reference wingtip displacements, measured by the MRS, are also subject to errors (such as tracking errors due to reflections from the transparent wing skin), which are not quantified here.

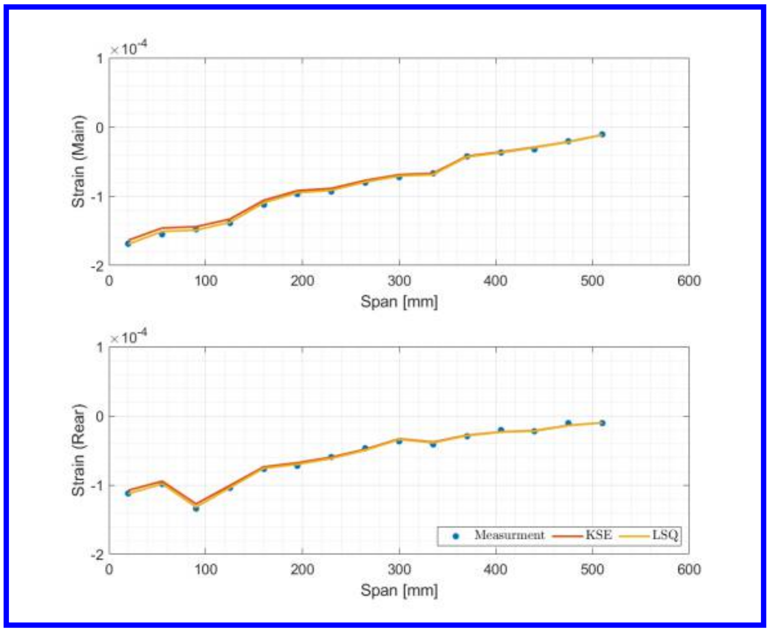

Fig. 8 Estimated spanwise strain distribution at t=1(s)

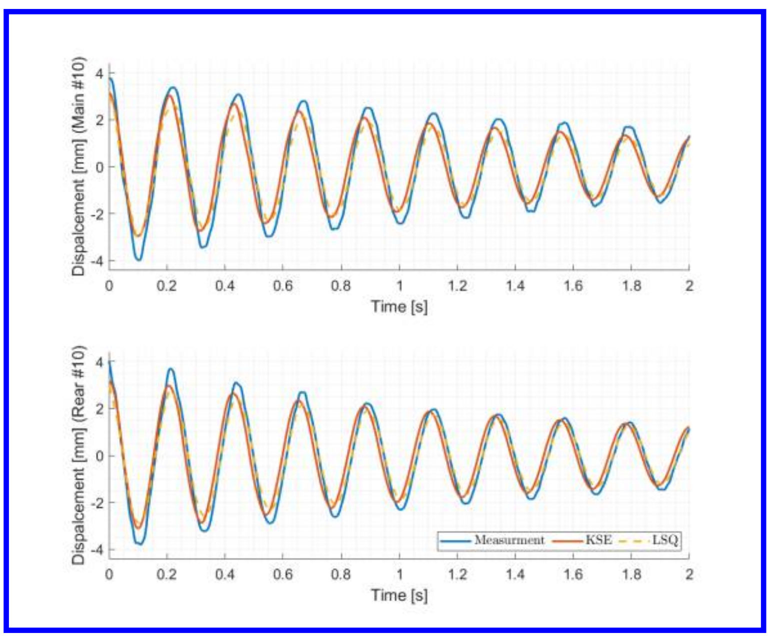

Fig. 9 Estimated wingtip displacements based on experimental strain modes and computational displacement modes

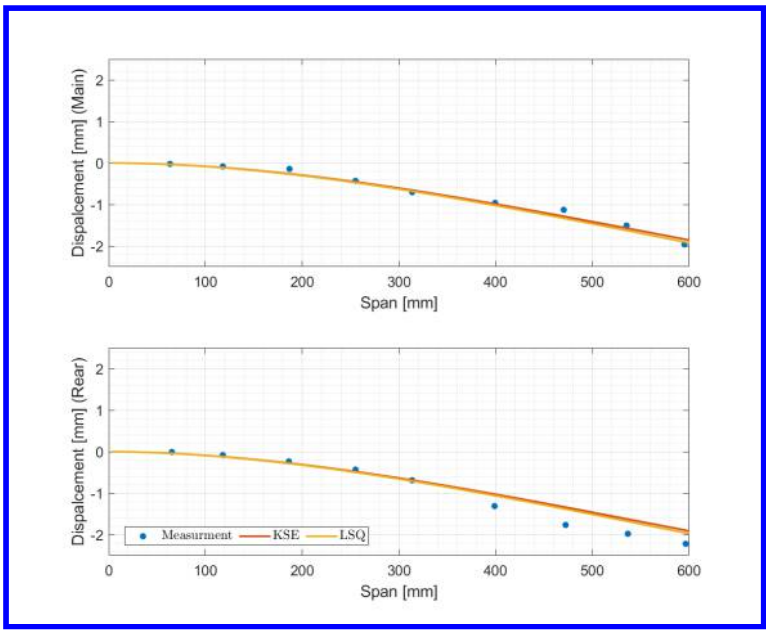

Fig. 10 Estimated wing shape at t=1(s) based on experimental strain modes and computational displacement modes

B. Aeroelastic Response

The wing was placed in the wind tunnel at the nominal airspeed of 20 (m/s) and zero degrees angle of attack, and was excited by all four control surfaces, simultaneously. Each control surface was moved harmonically, amplitude a_i, according to

$$\delta_{i\ com} = a_i \sin(0.5\pi t), \tag{21}$$

where

$$a = [0.02, 0.03, 0.07, 0.075], \tag{22}$$

and where i is the control-surface index, from root to tip. Strains and displacements were measured with the FOS and MRS setups presented in section III. The results show the reconstruction of the wing modal displacements, physical displacements, and strains based on the measured strain-data and the computational (from FE) displacement and strain modes. These are compared to measured quantities. Results are shown for the nominal case and also for cases in which 1) the strain sensors are saturated 2) the airspeed of the aeroelastic model is different than the test airspeed, and 3) both the strains are saturated there are differences in the airspeed between the model and test.

Figures 11 and 12 show the first four modal displacements in time as computed by the aeroelastic simulation and as estimated based on strain data via LSQ and the KSE. Figure 11 shows the whole time response and Figure 12 focuses on the two last cycles of excited response and the decay that follows (the time period in which there is no excitation but the airloads still drive the wing). For this nominal case, the $\boldsymbol{R}$ and $\boldsymbol{Q}$ matrices in the KSE gain are set as unit matrices. Figure 11 shows that the KSE tracks the modal displacement almost immediately.

The dominant modes in the response are the bending modes (first and second bending, ξ_1, and ξ_2). For these modes, there is an agreement between the simulation and LSQ responses, and therefor the KSE also yields similar modal responses. The torsion and lateral bending modal displacements, ξ_2 and ξ_3 are different between the simulation and LSQ, and the KSE weighs the two. We note that in the test, the bending motion has more dominant response in the first bending frequency, which the simulation does not predict. This is well captured by the measured strains and hence in the KSE and LSQ modal displacement estimates.

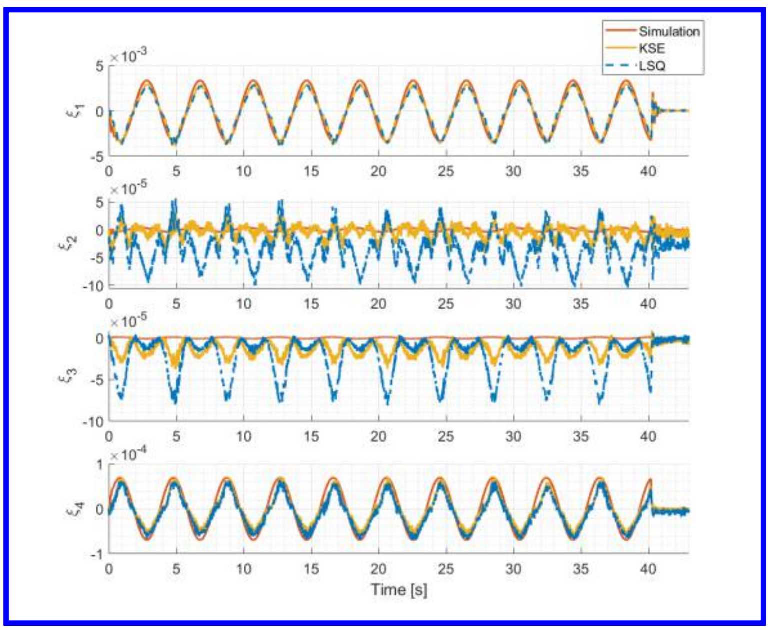

Fig. 11 Modal displacements estimation at nominal airspeed of 20 m/s

Figure 13 shows the strain in sensor #2 on the main and rear spars, comparing the simulation and the LSQ and KSE estimates to the experimentally measured data. We recall that the LSQ and KSE are based on measurements at sensors 1,4,7, and 10 only. The excellent agreement between the LSQ and measured strains indicates that when the strain data are good (i.e, no saturation or misreadings), the LSQ process completely recovers the strains. The simulation over-predicts the strain values. The KSE is in very good agreement with the measurement, with maximal errors of 95 $\mu\varepsilon$ and 62 $\mu\varepsilon$ for the two shown strains. Figure 13 also indicates that four modes are sufficient for strain reconstruction.

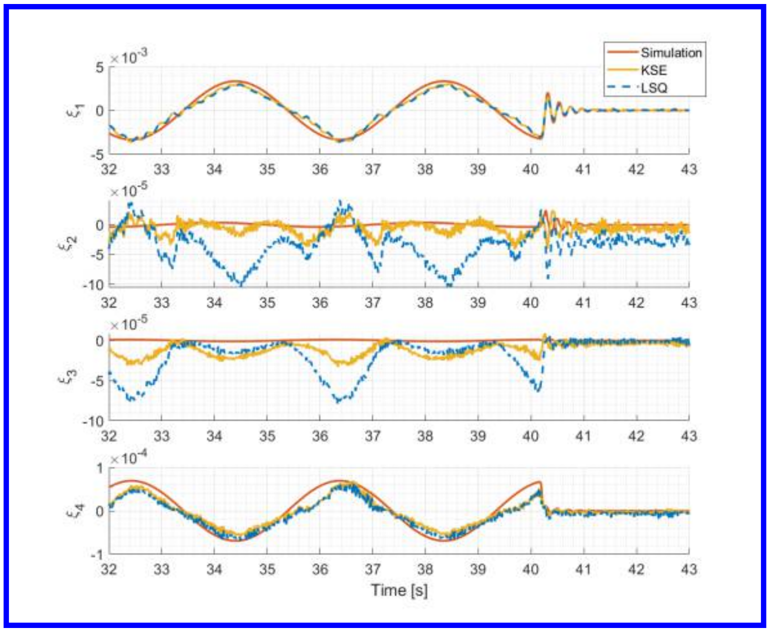

Fig. 12 Modal displacements estimation at nominal airspeed of 20 m/s (last two periods and decay)

Figure Figure 14 shows the wingtip displacements on the front and rear spars. Overall, there is a very good agreement between all results. The experimental data exhibits oscillations at the structural bending frequency, which are well captured by the KSE and LSQ, based on measured strains, but does not show in the simulation. We note that the MRS itself has tracking errors that are not quantified or accounted for here. This can explain the discrepancies between the measured displacements and the LSQ estimate. The results in this case show that when good strain data are available, the wing's response can be recovered via either LSQ or the KSE with high accuracy. The following example examines a realistic case of strain saturation or missing data.

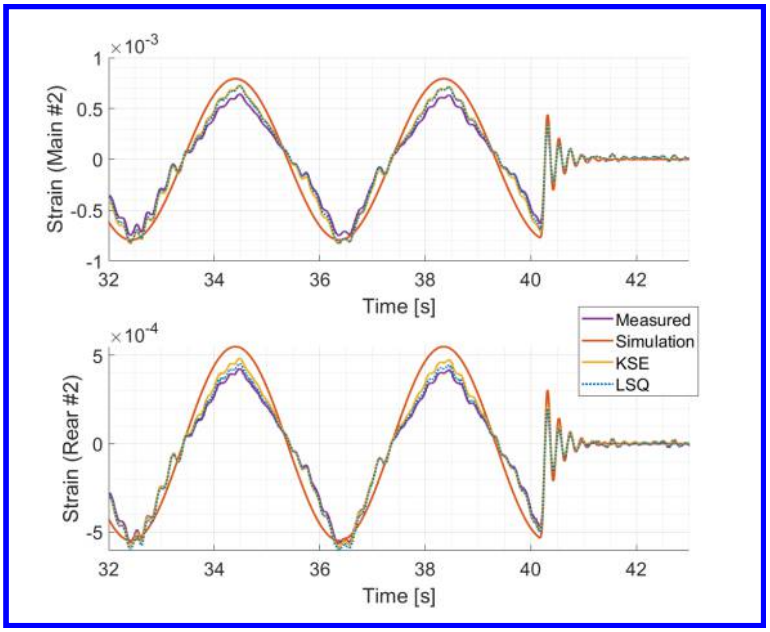

Fig. 13 Estimated wing's root strain at nominal airspeed of 20 m/s

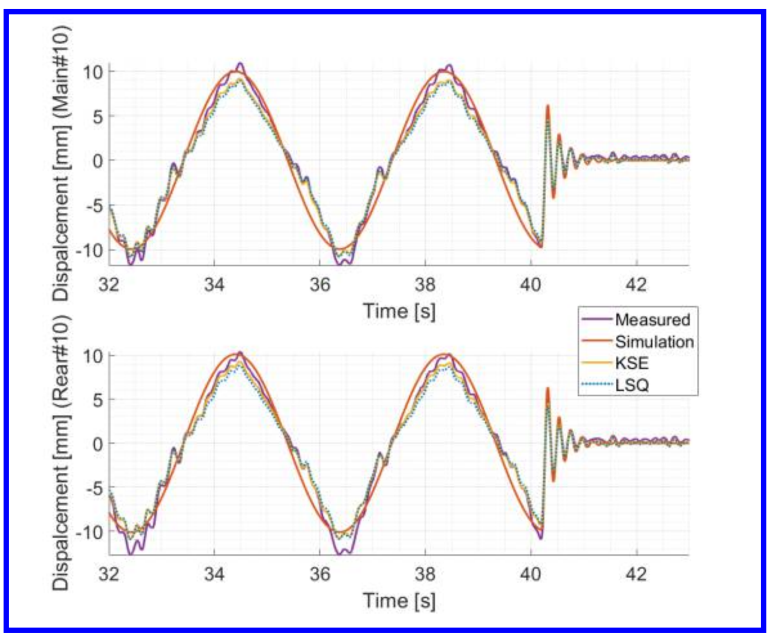

Fig. 14 Estimated wingtip displacements at nominal airspeed of 20 m/s

To examine the effect of strain-data saturation, we have artificially defined strain measurements saturation at $\pm 500\mu s$, for all sensors. The recovery of the modal displacements, physical displacements, and strains was repeated with the saturated data. The KSE measurement-noise covariance matrix $\boldsymbol{R}$ values were updated during the simulation as described in section Section III.A.

Figure 15 shows the four modal displacements, comparing the simulation, LSQ, and KSE results. The strain-saturation does not affect the recovery of the first, dominant, bending mode significantly. However, it does affect the second bending mode, ξ_4. In this case, there is a large discrepancy between the LSQ and the simulation at saturation times and the KSE is correlated with the simulation (thanks to the adjustment of $\boldsymbol{R}$). Figure 16 shows the measured,

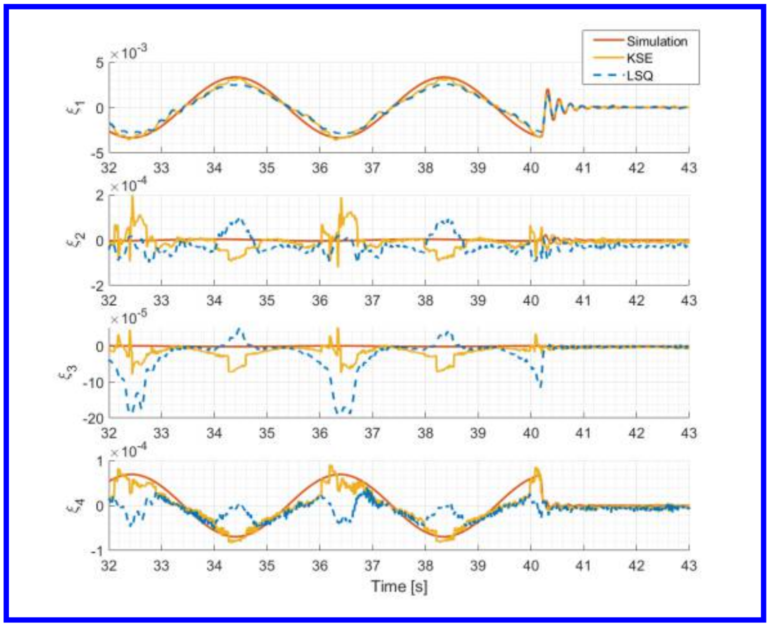

Fig. 15 Modal displacements estimation at nominal airspeed with measurement saturation

measured and artificially saturated, simulated, and LSQ and KFE recovered strains at strain sensor #1, closest to the root. This is one of the strain sensors that were used for the modal displacement estimate. Figure 16 shows how the KSE accurately recovers the measured strain even at times of saturated measurement. On the rear spar, the strains are only saturated at the negative values and for short periods of time. Some oscillations in the KSE responses occur at times of KSE parameters adjustments. Figure 17 shows displacement recovery. Here, the KSE recovers the displacement trends much better than the LSQ process that is directly affected by the strain saturation.

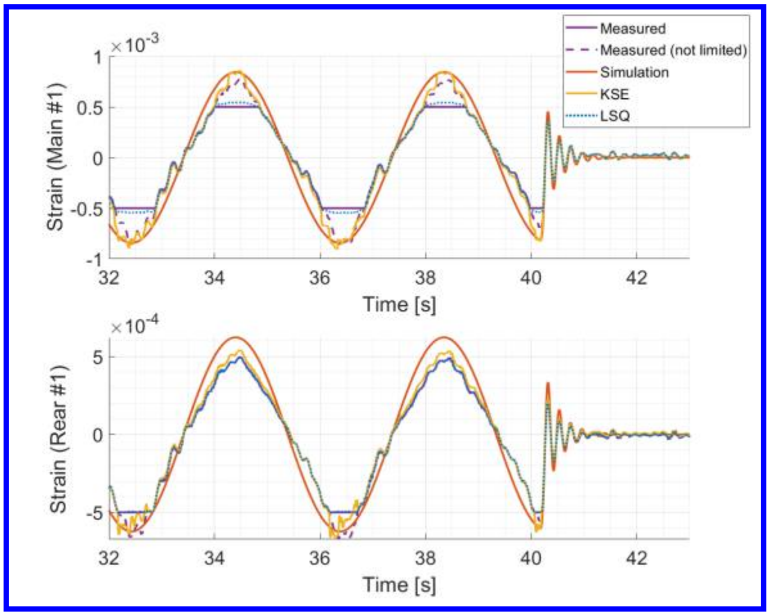

Fig. 16 Estimated wing's root strain at nominal airspeed with measurement saturation

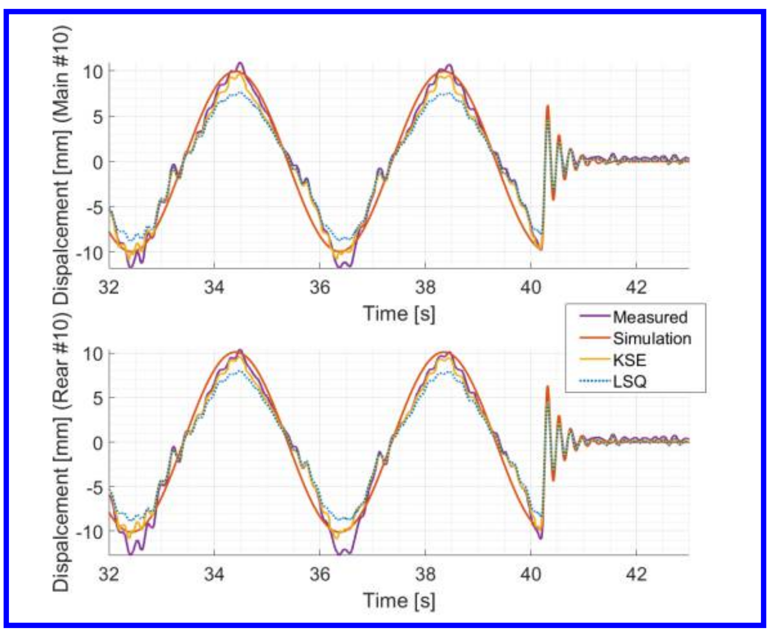

Fig. 17 Estimated wingtip displacements at nominal airspeed with measurement saturation

We have demonstrated that when good, continuous strain data is available, it can be used to accurately estimate the displacements. In times of damaged or missing data, the KSE, supported by the computational model, can compensate for data loss and still provide a good estimate of the displacements. The KSE relies on an aeroelastic model, which varies with the airspeed. Several models, for different airspeeds, can be used and switched between according to the actual flight speed. However, it is likely that the actual flight speed will not coincide with one of the airspeeds for which an aeroelastic model was generated. In such a case, we use the KSE with the process noise covariance matrix $\boldsymbol{Q}$ as in Eq. 20. Figure 18 shows displacements at $20/m/s$ from LSQ and from KSE, based on an aeroelastic model for $23/m/s$, using the nominal and modified $\boldsymbol{Q}$ matrix. Good estimate of the displacements is achieved by the KSE with the adjustment of the process noise covariance.

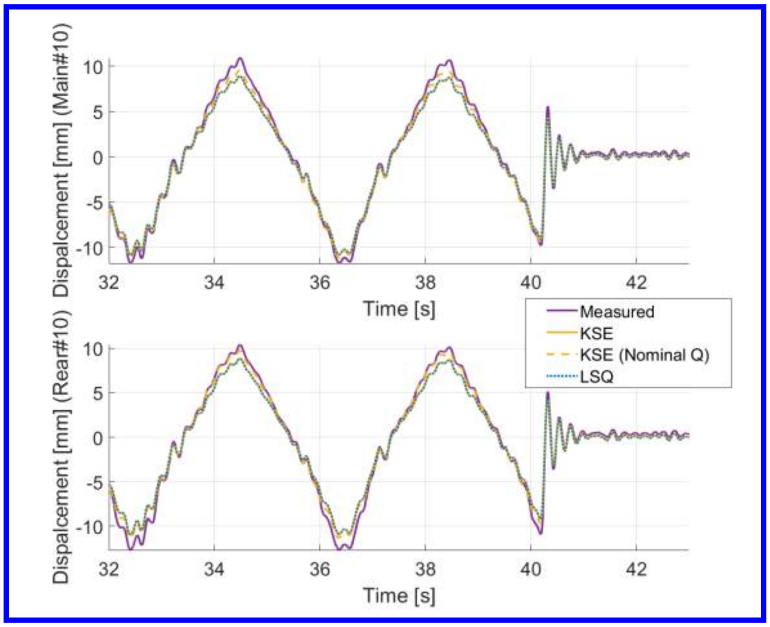

Fig. 18 Estimated wingtip displacements at airspeed of 20 m/s from LSQ and from KSE based on an aeroelastic model at 23 m/s

V. Summary

The paper presented a new method for shape sensing of a flexible wing that is based on strain data and makes use of the Kalman state estimator (KSE). The method was tested experimentally on a test case of a flexible wing, equipped with four control surfaces. Strain data was collected at 30 locations over the wing's front and rear spars by Fiber Bragg Grating sensors embedded in two optical fibers. Reference wing deformation data was collected by a motion recovery camera system (MRS). Two cases were studied, of recovering the wing's dynamic deformations in 1) Structural response to a hammer hit and 2) Aeroelastic response to excitation by the control surfaces in the wind tunnel, at airspeed of 20 m/s. The collected strain data were used to extract the modal and physical deformations and strain values at unmeasured locations. The estimates by the were compared to those from a modal-based least-squares (LSQ) method.

For the structural response case, it was shown that the KSE closely follows the deformations and provides an accurate estimate of the strain at unmeasured locations. Compared with the LSQ procedure, it has the advantage that the modal velocities are estimated together with the modal displacements. Thus, the KSE also provides a smooth prediction of the modal velocities, which can be used for control. In the wind-tunnel test, modal and physical deformations were computed by the KSE and compared to those from aeroelastic simulation, from the LSQ method, and to the reference deformations as measured by the MRS. It was shown that when the strain data from the optical fibers is fully available, it is of high quality and thus the LSQ method accurately computed the deformations. In such cases, the KSE can be adjusted to yield the exact same results as the LSQ, by setting the noise covariance matrix in the KSE gain to zero. When the strain data is corrupt (e.g., due to sensor saturation) or is temporarily unavailable, the KSE can still provide good deformation estimates by relying heavier on the model. The KSE was shown to provide good deformation estimates even when the underlying aeroelastic model was generated for an airspeed different than that in the test. Overall, the

KSE, weighing together an aeroelastic model and measurements, provides a reliable approach to flexible wing shape sensing in the wind tunnel or flight. It can be adjusted in real-time to account for gaps or errors in the measurements (strain data) and provide a good estimate of the modal displacements and velocities for flight control.

References

[1] Reich, G., Raveh, D., and Zink, P., "Application of Active-Aeroelastic-Wing Technology to a Joined-Wing Sensorcraft," *Journal of Aircraft*, Vol. 41, No. 3, 2004.

[2] Suh, P., Chin, A., and Mavris, D., "Virtual Deformation Control of the X-56A Model with Simulated Fiber Optic Sensors," Tech. rep., NASA, 2014. NASA/TM—2014–216616.

[3] Yagil, L., Raveh, D. E., and Idan, M., "Deformation Control of Highly Flexible Aircraft in Trimmed Flight and Gust Encounter," *Journal of Aircraft*, Vol. 55, No. 2, 2018, pp. 829–840.

[4] Pak, C., "Wing Shape Sensing from Measured Strain," *AIAA Journal*, Vol. 54, No. 3, 2016, pp. 1068–1077.

[5] Gherlone, M., Cerracchio, P., and Mattone, M., "Shape Sensing Methods: Review and Experimental Comparison on a Wing-Shaped Plate," *Progress in Aerospace Sciences*, Vol. 99, 2018, pp. 14–26.

[6] Freydin, M., Rattner, M. K., Raveh, D. E., Kressel, I., Davidi, R., and Tur, M., "Fiber-Optics-Based Aeroelastic Shape Sensing," *AIAA Journal*, Vol. 57, No. 12, 2019, pp. 5094–5103.

[7] Todd, M., Malsawma, L., Chang, C., and Johnson, G., "The Use of Fiber Bragg Grating Strain Sensors in Laboratory and Field Load Tests: Comparison to Conventional Resistive Strain Gages," Tech. rep., Naval Research Laboratory Washington DC, 1999.

[8] Ko, W. R., William L., and Tran, V. T., "Displacement Theories for In-Flight Deformed Shape Predictions of Aerospace Structures," Tech. rep., NASA, 2007. NASA/TP-2007-214612.

[9] Tessler, A., and Spangler, J. L., "A Variational Principle for Reconstruction of Elastic Deformations in Shear Deformable Plates and Shells," Tech. rep., NASA, 2003. NASA/TM—2003-212445.

[10] Gherlone, M., Cerracchio, P., Mattone, M., Di Sciuva, M., and Tessler, A., "An Inverse Finite Element Method for Beam Shape Sensing: Theoretical Framework and Experimental Validation," *Smart Materials and Structures*, Vol. 23, No. 4, 2014, p. 045027.

[11] Foss, G. C., and Haugse, E. D., "Using Modal Test Results to Develop Strain to Displacement Transformations," *Proceedings - SPIE The International Society for Optical Engineering*, SPIE International Society for Optical Engineering, 1995, pp. 112–112.

[12] Kalman, R. E., "A New Approach to Linear Filtering and Prediction Problems," *Journal of Basic Engineering*, Vol. 82, No. 1, 1960, pp. 35–45.

[13] Rajendra P. Palanisamya, H. K., Soojin Cho, and Simc, S.-H., "Experimental Validation of Kalman Filter-Based Strain Estimation in Structures Subjected to Non-Zero Mean Input," *Smart Structures and Systems*, Vol. 15, No. 2, 2015.

[14] Karpel, M., Moulin, B., and Chen, P., "Dynamic Response of Aeroservoelastic Systems to Gust Excitation," *Journal of Aircraft*, Vol. 42, No. 5, 2005, pp. 1264–1272.

[15] Kang, L., Kim, D., and Han, J., "Estimation of Dynamic Structural Displacements Using Fiber Bragg Grating Strain Sensors," *Journal of sound and vibration*, Vol. 305, No. 3, 2007, pp. 534–542.

[16] Towne, A., Schmidt, O. T., and Colonius, T., "Spectral Proper Orthogonal Decomposition and Its Relationship to Dynamic Mode Decomposition and Resolvent Analysis," *Journal of Fluid Mechanics*, Vol. 847, 2018, pp. 821–867.

[17] Corp, M. S., *MSC Nastran Quick Reference Guide*, 2014.

[18] *ZAero User Manual V. 9.2*, Scottsdale, AZ, 3rd ed., 2017.